

GRAPH-BASED EVENT FINGERPRINTS FOR CLASSIFYING GEOMAGNETIC STORM-DRIVEN FORBUSH DECREASES

JUAN D. PEREZ-NAVARRO^{a,*} 

Universidad Tecnológica de Bolívar. Escuela de Transformación Digital. Parque Industrial y Tecnológico Carlos Vélez Pombo Km 1 Vía Turbaco. Cartagena de Indias, 130010, Colombia and

* Corresponding author: perezjuan@utb.edu.co (Juan D. Perez-Navarro)

D. SIERRA-PORTA^{a,***} 

Universidad Tecnológica de Bolívar. Escuela de Transformación Digital. Parque Industrial y Tecnológico Carlos Vélez Pombo Km 1 Vía Turbaco. Cartagena de Indias, 130010, Colombia and

** Corresponding author: dporta@utb.edu.co (D. Sierra-Porta)

Version February 19, 2026

Abstract

Forbush decreases (FDs) are transient depressions in the galactic cosmic-ray flux observed by global neutron-monitor networks and are commonly associated with interplanetary disturbances driven by coronal mass ejections and related shocks. Despite extensive observational work, quantitatively comparing FD morphology across events and linking it to storm severity remains challenging due to heterogeneous station responses, coverage gaps, and the multivariate nature of the network. This work introduces a graph-based event representation in which each FD is mapped to an event network constructed from pairwise dissimilarities between station response time series. A controlled sparse backbone is obtained via the minimum spanning tree, enabling comparable event graphs across cases. From each graph, a compact set of geometric/topological fingerprints is computed, including global integration measures, spectral summaries, mesoscopic structure, centrality aggregates, and complexity descriptors.

Predictive skill is assessed using strict leave-one-event-out validation over a pre-defined grid of distance metrics and distance-domain transformations, with selection criteria fixed *a priori*. The proposed fingerprints exhibit measurable signal for three tasks: (i) multi-class classification of geomagnetic storm intensity (G3/G4/G5) with moderate but consistent performance and errors dominated by adjacent categories; (ii) stronger binary severity screening (\geq G4 vs. G3) with high sensitivity to severe events; and (iii) drop regression with partial least squares achieving positive explained variance relative to a fold-wise mean baseline. These results support the premise that FD event morphology leaves reproducible network signatures that can be captured by compact graph fingerprints, offering a complementary, interpretable framework for comparative FD characterization and for studying how heliospheric drivers imprint structure on global neutron-monitor responses.

Subject headings: Forbush decrease – space weather – neutron monitor – network graph

1. INTRODUCTION

Forbush decreases (FDs) are transient reductions in the galactic cosmic-ray (GCR) flux observed at Earth (Chilingarian *et al.* 2022). The physical mechanism behind Forbush decreases involves the magnetic field of plasma solar wind sweeping galactic cosmic rays away from Earth (Ghosh and Raychaudhuri 2007; Cane 2000). These events are associated with large-scale perturbations in the solar wind and interplanetary magnetic field, particularly non-recurrent decreases that are caused by transient interplanetary events related to coronal mass ejections from the Sun (Blanco *et al.* 2013; Huang *et al.* 2017).

Because neutron monitors register the integrated response of secondary particles generated in the atmo-

sphere, FD signatures are routinely tracked in multi-station networks, and they remain a standard observable for studying the coupling between interplanetary transients and near-Earth particle environments (Chilingarian *et al.* 2025; Bahena Bias and Villaseñor 2011; Paiaioannou *et al.* 2013). Despite decades of observational work, robust event-level characterization across stations continues to face practical challenges: FD morphologies vary with event type, viewing geometry, background conditions, and data completeness, while station responses differ systematically across the global network.

A key driver of inter-station heterogeneity is geomagnetic shielding. Station cutoff rigidity determines the minimum particle rigidity required to reach a given detector and therefore modulates both FD amplitude and timing (Yushkov 2026). As a result, FD strength is not solely an intrinsic property of the interplanetary driver; it is also filtered by the spatial distribution of observing

stations and their rigidity thresholds (Laitinen and Dalla 2021; Ihongo *et al.* 2019; Okany 2025; Sierra-Porta and Domínguez-Monteroza 2022; Sierra-Porta 2024). This motivates analyses that explicitly combine multi-station measurements with station metadata rather than treating each time series in isolation. In practice, however, many studies focus on a limited number of stations, compress the network into summary curves, or rely on pairwise comparisons without a unifying representation that is directly comparable across events.

Graph-based representations provide a principled way to summarize multivariate observations (Freitas Silva *et al.* 2025, 2021). Nodes can represent stations and edges can encode inter-station similarity or dissimilarity, yielding an event-specific network that can be characterized by well-defined structural descriptors. In the context of FD observations, such representations offer a pathway to convert multi-station time series into compact event fingerprints that can be compared across drivers, storm intensities, and event magnitudes (Perez-Navarro and Sierra-Porta 2026). A central methodological issue is comparability: naive similarity thresholds often generate overly dense graphs that trivialize many network metrics, whereas overly aggressive pruning can distort the underlying organization (Gutierrez Gomez *et al.* 2017). A reproducible graph-based FD framework must therefore specify (i) the event window and missing-data treatment, (ii) the similarity/distance definition, and (iii) a graph-construction rule that yields interpretable and comparable connectivity across events.

This work introduces an event-level network construction for FDs observed in the Neutron Monitor Database (NMDB). For each event, stations are treated as nodes and edges are derived from pairwise dissimilarities between station response series within a common event window, with missing values handled through alternative, explicitly defined strategies (coverage-based station filtering or iterative imputation). In addition, transformations and optional scalings are applied in the distance domain to control dynamic range and enhance cross-event comparability. For visualization and controlled backbone comparison, minimum spanning trees (MST) are used to provide sparse (Stam *et al.* 2014), connected representations that highlight the dominant inter-station couplings while keeping the edge count fixed across events.

The scientific objective is to test whether graph fingerprints capture systematic differences between FD events stratified by geomagnetic storm intensity and by FD magnitude (drop). Three complementary predictive tasks are considered: multi-class intensity classification (G3/G4/G5), binary severity screening ($\geq G4$ vs. G3), and drop regression. Evaluation is performed under strict leave-one-event-out validation, and model selection is restricted to a pre-defined, theory-motivated grid of pipeline choices with selection criteria fixed *a priori*.

The contributions of this study are threefold. First, it provides a reproducible pipeline that maps multi-station FD time series into event graphs with explicit control of preprocessing, missing-data handling, and distance-domain operations. Second, it defines a compact set of graph descriptors spanning integration, spectral structure, mesoscopic organization, centrality aggregates, and complexity measures, enabling event-level analysis in small-sample regimes with leakage-free val-

idation. Third, it provides evidence that graph fingerprints derived from NMDB carry information about storm severity and FD magnitude and reveal rigidity-conditioned organization in representative event backbones, supporting graph-based characterization as a complementary tool for FD and space-weather studies.

2. DATA

We use neutron-monitor count-rate records from the NMDB, selecting the subset of stations available during each Forbush decrease (FD) event (Steigies 2023, 2016; Mavromichalaki *et al.* 2011). For each event, we extract a common analysis window around the disturbance and assemble a time-aligned matrix whose columns correspond to stations and whose rows correspond to measurement times. Station coverage varies across events due to data availability and quality control.

To characterize the magnitude of the event at each station, we used the calculation of the percentage reduction in the cosmic ray count rate with respect to a pre-event reference level which comes from the data metadata from NMDB and then visually confirmed from a curated review of each dataset.

Each FD event is associated with an externally defined classification of geomagnetic activity. We compile event labels from widely used FD catalogs and peer-reviewed studies, and we complement these labels with space-weather reports from operational sources, including NASA and GOES-based products when applicable. In this work, we focus on storm intensity classes (G_i , with $i = 2, 3, 4, 5$) as the primary categorical label, and we also retain event amplitude information derived directly from the neutron-monitor observations.

Finally, we collect station metadata from NMDB and associated station documentation, including cutoff rigidity, geographic coordinates (latitude and longitude), and altitude. These attributes are used both for descriptive analysis and to evaluate rigidity-conditioned network structure and node-level roles across events.

3. METHODS

3.1. Event windows and missing-data treatments

For each Forbush decrease (FD) event, a common analysis window is extracted from multi-station NMDB count-rate records and arranged into a time-aligned matrix $X \in \mathbb{R}^{T \times N}$, where T is the number of time samples and N is the number of stations available for that event.

A complementary missing-data treatments is considered to assess robustness. (i) Coverage filtering: stations whose fraction of missing values within the event window exceeds a fixed threshold $\tau = 0.5$ are excluded, and subsequent computations operate on the retained station set. (ii) Imputation: missing samples in X are imputed using an iterative multivariate scheme with a KNN ($k = 2$) regressor as the base estimator (Iterative Imputation), producing a complete matrix prior to distance estimation. These two treatments define alternative event representations and are treated as part of the pre-defined pipeline grid.

3.2. Pairwise distances between station responses

Let $\mathbf{x}_i \in \mathbb{R}^T$ denote the (possibly imputed) response series for station i in a given event window. Event-specific pairwise distances are computed between station

responses to form a matrix $D \in \mathbb{R}^{N \times N}$ with entries d_{ij} . Two ℓ_p distances are considered:

$$d_{ij}^{(p)} = \left(\sum_{t=1}^T |x_i(t) - x_j(t)|^p \right)^{1/p}, \quad (1)$$

where $p = 1$ corresponds to Manhattan distance, and $p = 2$ corresponds to the Euclidean member of the Minkowski family (Shirkhorshidi *et al.* 2015; Wang *et al.* 2021; Shifaz *et al.* 2023). This choice provides a parsimonious comparison between a more robust absolute-deviation geometry ($p = 1$) and a quadratic geometry ($p = 2$).

3.3. Distance-domain transformations and normalizations

To control dynamic range and improve comparability across events, additional operations are applied directly in the distance domain. Let t denote a robust scale defined as the median of the off-diagonal distances $\{d_{ij}\}_{i < j}$ for a given event. Three distance-domain transformations are explored:

$$\tilde{d}_{ij} = d_{ij} \quad (\text{none}), \quad (2)$$

$$\tilde{d}_{ij} = \log\left(\frac{d_{ij}}{t}\right) \quad (\text{log}), \quad (3)$$

$$\tilde{d}_{ij} = \exp\left(\frac{d_{ij}}{t}\right) \quad (\text{exponential}). \quad (4)$$

After transformation, an optional normalization is applied to \tilde{D} (e.g., none, min-max, z-score, robust scaling, or decimal scaling), yielding a final event-specific dissimilarity matrix used for graph construction.

3.4. Graph construction

Each event is represented as a weighted, undirected graph $G = (V, E, W)$ (Chung and Lu 2006; Kim and Wilhelm 2008) where nodes correspond to stations ($|V| = N$). Edges connect all station pairs (E is complete over the retained stations), and weights are given by the transformed/normalized dissimilarities ($w_{ij} = \tilde{d}_{ij}$). In this representation, smaller weights indicate stronger similarity (shorter dissimilarity). No additional edge sparsification is imposed; comparability across events is primarily enforced through the station-level coverage filtering and the distance-domain scaling described above.

A consistent visual pattern is a core-periphery organization in which intermediate-rigidity stations tend to occupy bridging positions, while very low-rigidity stations (polar/high-latitude, darker colors) more often appear as peripheral branches. High-rigidity stations (warmer colors) show partial clustering and connect through a small number of intermediates, suggesting that similarity in rigidity can translate into similarity of FD response morphology and, consequently, shorter dissimilarities. This qualitative behavior motivates rigidity-aware summaries such as assortativity and centrality-rigidity relations at the event level.

Figure 1 provides an illustrative event-level network visualization for a representative FD. Nodes correspond to neutron-monitor stations and node color encodes the

cutoff rigidity (GV). Edges correspond to the MST computed from the event-specific dissimilarity matrix, providing a sparse, connected backbone with fixed edge count ($N - 1$) and enabling direct visual comparison across distance metrics. The two vertical panels highlight that changing the distance metric (Manhattan vs. Minkowski) can alter the backbone geometry (e.g., hubness and branch structure) while preserving the main large-scale station groupings.

For the illustrated event (drop $\approx 10.4\%$), the backbone already exhibits coherent connectivity across multiple rigidity regimes, but with visible heterogeneity in node roles: some stations act as connectors across subgroups, while others remain weakly coupled and attach as leaves. Across the full event set, the regression analysis formally tests whether such global organization patterns (e.g., efficiency, spectral complexity, centrality aggregation, and mixing structure) carry predictive signal for drop magnitude beyond a fold-wise baseline, rather than relying on individual visual examples.

3.5. Event-level graph fingerprints

From each weighted event graph, a compact fingerprint vector is computed by aggregating node-level and spectral/mesoscopic properties into event-level descriptors. The reported feature set includes: global efficiency, Estrada index, modularity, assortativity, average Katz centrality, average closeness, average betweenness, and a Laplacian-based summary, together with additional complexity descriptors (entropy, a fractal-dimension estimate, and a Hurst exponent estimated via rescaled-range statistics).

When centrality measures depend on path lengths, weighted shortest paths are computed using the dissimilarity weights. Event-level centralities are obtained by averaging node-wise values, producing comparable scalars across events. These descriptors are designed to capture complementary aspects of global integration (efficiency), spectral complexity (Estrada), mesoscopic structure (modularity), mixing patterns (assortativity), and heterogeneity/complexity (entropy/fractal/Hurst) in the station-response network. For a description of these descriptors, metrics and markers see for example Omar and Plapper (2020) and references therein.

3.6. Event labels, predictive tasks, and evaluation protocol

Each FD event is assigned (i) a storm intensity label on the NOAA G-scale and (ii) a continuous magnitude label given by the observed FD drop (%). Three tasks are considered: multi-class intensity classification (G3/G4/G5), binary severity screening ($\geq G4$ vs. G3), and drop regression.

Model selection is performed over a pre-defined, theory-motivated grid of pipeline choices (missing-data treatment, distance metric, distance-domain transformation, and optional normalization). Selection criteria are fixed *a priori*: macro-F1 for classification and R^2 for regression. Predictive evaluation is carried out with strict leave-one-event-out (LOEO) validation. For regression, performance is additionally compared against a fold-wise mean-predictor baseline computed on each training fold.

4. RESULTS

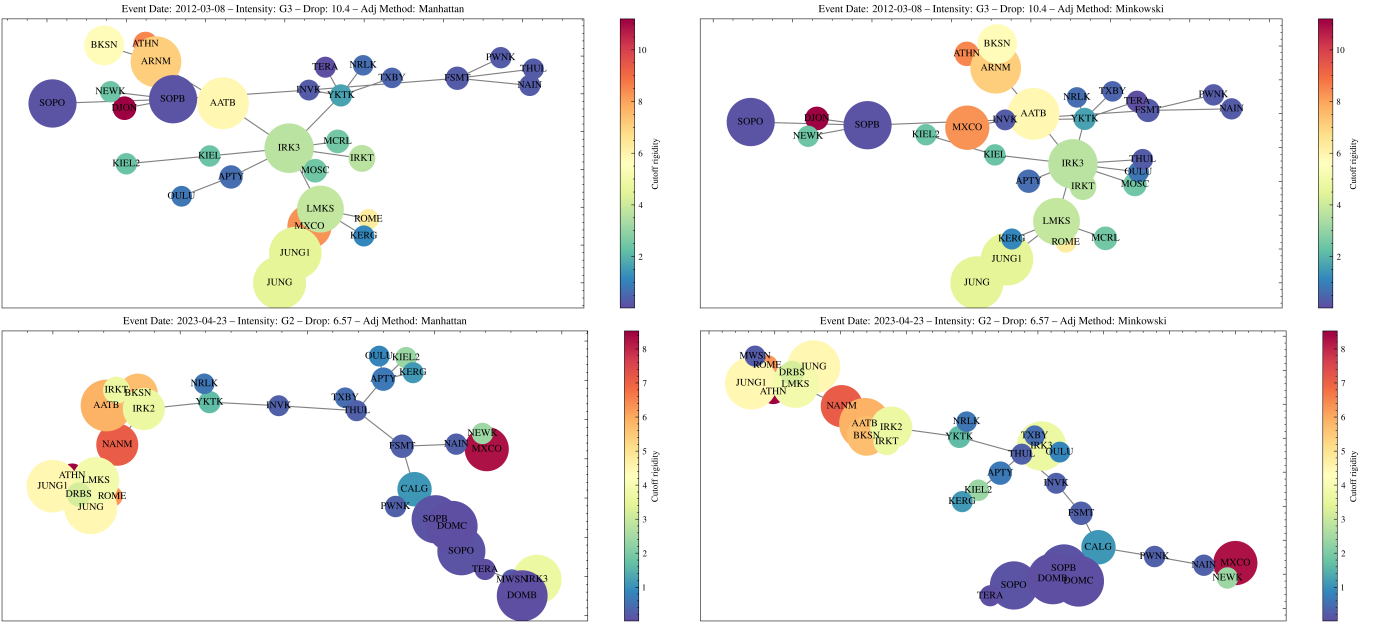


FIG. 1.— Illustrative two event graph for 2012-03-08 (G3) and 2023-04-23 (G2) from a representative Forbush decrease. Nodes are stations colored by cutoff rigidity (GV). Edges correspond to the MST computed from the event-specific dissimilarity matrix, yielding a sparse, connected backbone with $N - 1$ edges that minimizes total distance. Left: Manhattan ($p = 1$); right: Minkowski/Euclidean ($p = 3$). While the main station groupings persist, the MST topology (branching patterns and connector nodes) changes with the distance metric.

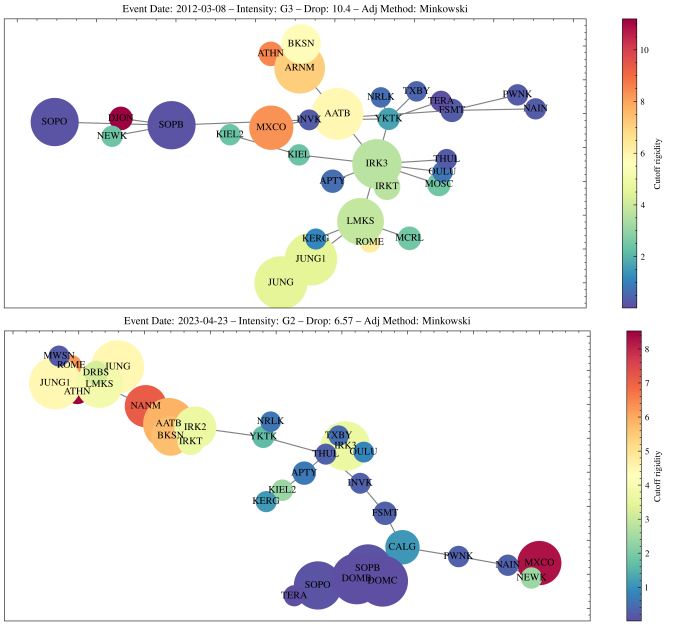
A model-selection stage was performed over a pre-defined and conceptually constrained set of graph-construction pipelines, combining (i) distance-domain transformations, (ii) standard normalization choices, and (iii) two adjacency metrics. Performance was assessed with a strict LOEO protocol; when needed, median imputation and standardization were fitted on the training fold only and applied to the held-out event, ensuring leakage-free evaluation. Selection criteria were fixed *a priori* (macro-F1 for classification; R^2 for regression) and applied over a small, theory-motivated grid of pipeline choices. For conciseness, only the best-performing configuration for each task is reported here; the full sweep across all tested combinations is available in the accompanying analysis notebook (and can be provided as supplementary material).

Given the strong class imbalance in the weakest category, the categorical intensity analysis focuses on G3/G4/G5; an additional binary screening task (\geq G4 vs. G3) is reported as an operationally meaningful complement.

4.1. Rigidity-conditioned node roles in event graphs

To assess whether geomagnetic shielding shapes *local* station roles within event graphs, node-level descriptors were stratified by cutoff rigidity and summarized across events. Stations were grouped into three rigidity bands using fixed physical thresholds: low rigidity ($R_c < 3$ GV), high rigidity ($R_c \geq 6$ GV), and an intermediate group spanning $3 < R_c < 6$ GV. For each event, node metrics were aggregated within each band to obtain group-level summaries, and the resulting distributions across events were compared.

Figure 2 shows the across-event distributions for four representative descriptors (avg. katz, avg. closeness, avg. betweenness, and a Laplacian-based summary). A clear separation by rigidity emerges. Low-rigidity



stations exhibit systematically larger avg. katz and avg. closeness across events, indicating that these stations tend to occupy more central positions in the event-network backbone and contribute disproportionately to global communicability-like structure. In the same group, avg. betweenness is also markedly higher, suggesting that low-rigidity stations more frequently act as bridges connecting subnetworks (or branches) in the backbone representation. Conversely, medium- and high-rigidity groups show substantially lower centrality levels, consistent with a more peripheral or locally confined role.

The Laplacian-based summary displays a complementary behavior, with the intermediate-rigidity group exhibiting larger values and broader variability than the low- and high-rigidity groups (Figure 2). Although Laplacian-derived measures admit multiple interpretations depending on the specific definition used, this pattern is compatible with the idea that intermediate-rigidity stations often mediate connectivity between the strongly modulated low-rigidity responses and the more weakly modulated high-rigidity responses, thereby shaping the graph's diffusion-/spectral-like organization. Taken together, these results provide event-level evidence that cutoff rigidity conditions node roles in a reproducible way and motivate rigidity-aware descriptors as interpretable components of FD graph fingerprints. Notably, two metrics exhibiting strong rigidity separation here (avg. katz and avg. laplacian) also rank among the most influential predictors in the intensity classification models (Table 4), linking physical interpretability and predictive performance.

4.2. Multi-class classification of storm intensity (G3/G4/G5)

The main classification task targets the categorical storm intensity associated with each Forbush event (G3/G4/G5). The best multi-class result was obtained

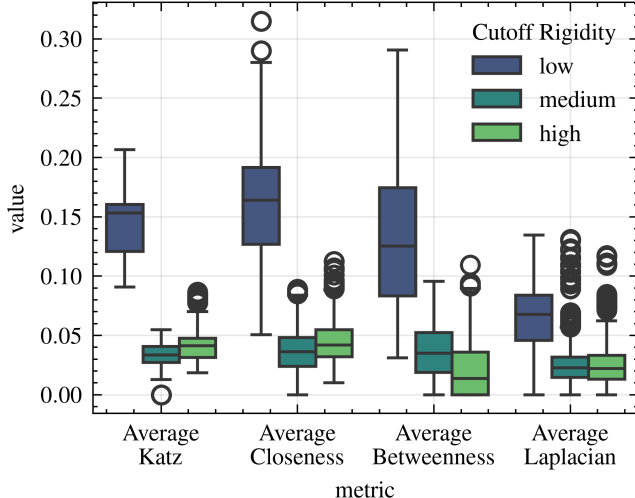


FIG. 2.— Rigidity-conditioned distributions of node-role summaries across events. For each FD event graph, node-level metrics are aggregated within three cutoff-rigidity bands defined by fixed thresholds: low ($R_c < 3$ GV), medium ($3 \leq R_c < 6$ GV), and high ($R_c \geq 6$ GV). Boxplots summarize the distributions across events. Low-rigidity stations show systematically larger avg. katz, avg. closeness, and avg. betweenness, indicating more central and bridging roles in event backbones, while the Laplacian-based summary peaks for the medium-rigidity group.

using a log transformation in the distance domain, no post-distance normalization, and Minkowski-based adjacency, followed by linear discriminant analysis. Under LOEO ($n = 33$ events), the classifier achieved an accuracy of 0.576, balanced accuracy of 0.572, and macro-F1 of 0.575.

Table 1 reports the confusion matrix. Class-wise recalls are $\text{Rec}_{G3} = 6/10 = 0.60$, $\text{Rec}_{G4} = 8/13 = 0.62$, and $\text{Rec}_{G5} = 5/10 = 0.50$, indicating that performance is not driven by a single class. Misclassifications are dominated by neighboring categories (notably $G4 \leftrightarrow G5$), consistent with the expectation that storm severity forms a continuum and that graph fingerprints may partially overlap when intensities are close in magnitude. Figure 3 visualizes the same configuration in discriminant space (LD1–LD2), showing a moderate but nontrivial organization by intensity.

TABLE 1
LOEO CONFUSION MATRIX FOR THE BEST MULTI-CLASS INTENSITY MODEL (LDA; G3/G4/G5; $n = 33$).

	Pred G3	Pred G4	Pred G5
True G3	6	1	3
True G4	1	8	4
True G5	2	3	5

4.3. Binary severity screening: $\geq G4$ versus $G3$

A binary severity screening task was also considered, grouping strong storms (G4/G5) versus moderate storms (G3), using the same best-performing graph-construction setting as above. Under LOEO ($n = 33$), LDA achieved an accuracy of 0.758, balanced accuracy of 0.685, and macro-F1 of 0.694 (Table 2).

Sensitivity to severe events is high: the true positive rate for $\geq G4$ is $20/23 = 0.87$. Specificity for G3 is

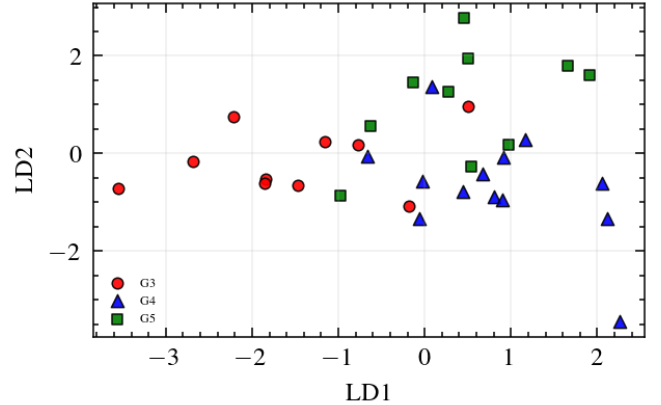


FIG. 3.— LDA projection (LD1–LD2) for the best multi-class intensity pipeline (log distance transform, no normalization and Minkowski adjacency). Colors indicate storm classes (G3/G4/G5). lower ($5/10 = 0.50$), indicating that a subset of moderate events remains difficult to separate from the severe group. This asymmetry is consistent with the expectation that stronger disturbances imprint more distinctive global network signatures, while moderate events can occupy an intermediate regime in which fingerprints overlap with adjacent categories.

TABLE 2
LOEO CONFUSION MATRIX FOR BINARY SEVERITY SCREENING (LDA; $\geq G4$ vs. G3; $n = 33$).

	Pred G3	Pred $\geq G4$
True G3	5	5
True $\geq G4$	3	20

4.4. Drop regression with PLS (5 components)

The regression task evaluates whether graph fingerprints encode quantitative information about Forbush magnitude by predicting the observed drop (%). The best performance was obtained with Minkowski-based adjacency and no distance transformation or normalization, combined with partial least squares regression (PLS) using 5 components. Under LOEO ($n = 34$), the model achieved $R^2 = 0.350$, MAE = 2.41 percentage points, and RMSE = 3.06.

This outperformed a fold-wise mean-predictor baseline (LOEO), which yielded $R^2 = -0.062$, MAE = 2.69, and RMSE = 3.91. Figure 4 shows predicted versus observed drops, indicating measurable skill together with a typical regression-to-the-mean pattern: very large drops are underpredicted and small drops slightly overpredicted, which is expected given the limited sample size and the intrinsic variability linking event morphology to magnitude.

4.5. Summary of best configurations

Table 3 summarizes the best-performing configurations and LOEO performance. Overall, the results support the hypothesis that geometric/topological graph fingerprints extracted from multi-station Forbush observations contain reproducible signal for (i) stratifying storm intensity and (ii) partially explaining drop magnitude. Given the modest number of events, these findings are best interpreted as evidence of signal in the proposed fingerprints

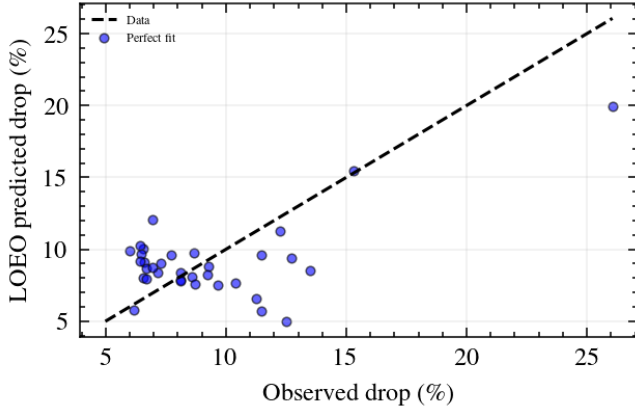


FIG. 4.— PLS (5 components) LOEO regression: predicted vs. observed Forbush drop (%) for the best pipeline (no transform; no normalization; Minkowski adjacency). The dashed line indicates perfect agreement.

rather than as a final operational model; larger event sets will enable tighter uncertainty quantification and more definitive benchmarking.

TABLE 3
BEST-PERFORMING CONFIGURATIONS (SELECTED BY LOEO PERFORMANCE) FOR EACH TASK.

Task	Best setting	LOEO performance
Multi-class intensity (G3/G4/G5)	LDA; log distance transform; no normalization; Minkowski adjacency	Acc = 0.576; Balanced Macro F1 = 0.572; Macro F1 = 0.575 ($n = 33$)
Binary severity ($\geq G4$ vs. G3)	LDA; LOG Normalización; Decimal Scaling; Minkowski adjacency	Acc = 0.7878; Balanced Acc = 0.7347; MacroF1 = 0.7413 ($n = 33$)
Drop regression	PLS-5; no transform; no normalization; Minkowski adjacency	$R^2 = 0.350$; MAE = 2.41; RMSE = 3.06 ($n = 34$)

4.6. Which graph descriptors drive the predictions?

To improve interpretability, descriptor relevance was estimated for the best-performing models by aggregating standardized coefficients across LOEO folds (Table 4). For multi-class intensity classification (G3/G4/G5), the dominant contributors were average Katz centrality (avg_katz), followed by the Estrada index, Laplacian-based summaries (avg_laplacian), entropy, and modularity. This ranking suggests that severity stratification is primarily supported by a combination of communicability-like/global connectivity structure (avg_katz), spectral organization (Estrada and Laplacian summaries), complexity/heterogeneity (entropy), and mesoscopic organization (modularity).

For the binary severity screening task ($\geq G4$ vs. G3), the same core set remains dominant (Table 4), with avg_katz again ranking first, followed by avg_laplacian, entropy, Estrada index, and modularity. The improved separation observed in the binary setting is therefore consistent with stronger shifts in global connectivity/communicability and distance-geometry/spectral structure between moderate and severe events, complemented by complexity and community organization.

For drop regression (PLS-5), the largest standardized coefficients were associated with assortativity (positive)

TABLE 4
MOST INFLUENTIAL GRAPH DESCRIPTORS FOR THE BEST-PERFORMING MODELS, ESTIMATED BY AGGREGATING STANDARDIZED COEFFICIENTS ACROSS LOEO FOLDS. FOR CLASSIFICATION, VALUES REPORT MEAN \pm STD RELEVANCE SCORES; FOR REGRESSION, COEFFICIENTS ARE REPORTED AS MEAN \pm STD (STANDARDIZED).

Task	Top descriptors (ranked)
G3/G4/G5 (LDA)	avg_katz (7.23 \pm 1.05), estrada_index (4.98 \pm 0.62), avg_laplacian (4.56 \pm 0.57), entropy (4.04 \pm 0.54), modularity (2.76 \pm 0.48)
$\geq G4$ vs G3 (LDA)	avg_katz (20.21 \pm 3.64), avg_laplacian (12.23 \pm 1.48), entropy (10.77 \pm 1.36), estrada_index (8.08 \pm 1.05), modularity (6.38 \pm 0.90)
Drop (PLS-5)	assortativity (+4.41 \pm 0.27), avg_betweenness (-4.34 \pm 0.25), modularity (-0.65 \pm 0.09), fractal (-0.65 \pm 0.10), avg_laplacian (-0.57 \pm 0.09)

and average betweenness (negative), followed by smaller but consistent contributions from modularity, fractal-dimension estimates, and Laplacian summaries (mostly negative; Table 4). This pattern indicates that drop magnitude is more strongly linked to mixing and bridging structure (assortativity and betweenness), with additional modulation from global organization and complexity captured by mesoscopic and spectral/complexity descriptors.

5. DISCUSSION

The results indicate that event-level graph fingerprints derived from multi-station neutron-monitor responses encode reproducible information about both geomagnetic-storm severity and Forbush magnitude. The moderate yet consistent performance in the G3/G4/G5 task, together with confusion dominated by adjacent categories, supports a physically plausible picture in which storm intensity behaves as an ordered continuum rather than a set of sharply separated regimes (NOAA Space Weather Prediction Center 2024). In this context, the LDA projection reveals partial organization in discriminant space, while overlap remains expected due to shared heliospheric drivers and heterogeneous station responses modulated by geomagnetic shielding (Cane 2000; Richardson and Cane 2011; Smart and Shea 2005).

The stronger performance observed in the binary screening task ($\geq G4$ vs. G3) suggests that the proposed fingerprints are particularly sensitive to the structural signatures of more intense disturbances. This behavior is consistent with the expectation that stronger CME/shock-driven transients can produce more coherent and global organization across stations, whereas moderate events may occupy an intermediate regime in which morphology overlaps with neighboring categories. The observed asymmetry between sensitivity and specificity further motivates reporting both multi-class stratification (for physical gradation) and binary screening (for robust detection of stronger events).

The regression results demonstrate measurable skill for predicting FD drop relative to a fold-wise mean baseline, indicating that global network organization carries quantitative information about event magnitude. The residual regression-to-the-mean pattern for extremes is consistent with limited sample size and with the intrinsically noisy mapping between response morphology and mag-

nitude when station coverage, rigidity distribution, and event geometry vary across cases (Mishev *et al.* 2024). These considerations suggest that drop prediction is feasible but likely benefits from larger event sets and additional physically informed covariates.

An additional point concerns representation choices in the distance domain. The configuration that maximized intensity classification favored a log transform, which is compatible with stabilizing topology- and centrality-based summaries by compressing the distance dynamic range and reducing the influence of outliers (Box and Cox 1964). In contrast, the best-performing regression configuration favored leaving distances untransformed, suggesting that absolute dissimilarity magnitudes can retain information relevant to drop that may be attenuated by aggressive scaling. This divergence reinforces that different scientific targets (categorical severity versus continuous magnitude) can prefer different representations, and that distance-domain operations should be treated as explicit modeling choices rather than purely technical preprocessing steps.

Finally, the MST backbone provides a controlled sparse, connected representation that improves comparability across events. This choice also mitigates well-known sensitivity of many network metrics to graph density when graphs are produced by naive thresholding. At the same time, the absence of cycles by construction implies that some mesoscopic descriptors are effectively probed through global and spectral summaries rather than through dense clustering structure. This motivates targeted future tests with fixed-density augmentations (e.g., MST plus a small number of shortest non-tree edges) to quantify the incremental value of cyclic structure while preserving cross-event comparability (Tumminello *et al.* 2007).

6. CONCLUSIONS AND OUTLOOK

A graph-based approach was developed to characterize Forbush decreases using event-level networks constructed from pairwise dissimilarities between station response series. A controlled sparse backbone (minimum spanning tree) yields comparable connected graphs across events, from which compact geometric/topological fingerprints are computed. Model selection was performed over a pre-defined, theory-motivated grid of pipeline choices, with selection criteria fixed *a priori* (macro-F1 for classification; R^2 for regression) and evaluation carried out under strict LOEO validation.

The main findings are: (i) multi-class intensity classification (G3/G4/G5) exhibits moderate but consistent skill, with errors dominated by neighboring categories, supporting a continuum-like interpretation of storm severity in fingerprint space; (ii) binary severity screening ($\geq G4$ vs. G3) yields stronger discrimination and high sensitivity to severe events, indicating potential utility for robust event triage; (iii) drop regression

demonstrates measurable predictive skill relative to a fold-wise mean baseline, implying that global network organization encodes quantitative information about FD magnitude, albeit with regression-to-the-mean tendencies for extremes.

Given the modest number of labeled events, these results are best interpreted as evidence of reproducible signal in the proposed fingerprints rather than as a final operational model. Several directions can strengthen both statistical confidence and physical interpretability: (a) **Larger and more diverse event sets:** expand the labeled catalog to stabilize model selection, enable calibration across solar-cycle phases, and support ordinal or cost-sensitive formulations aligned with the ordered nature of intensity classes; (b) **Uncertainty-aware benchmarking:** report confidence intervals via event-level resampling (bootstrap) and assess robustness under alternative splits (e.g., leave-one-year-out or leave-one-solar-cycle-out) when sample size permits; (c) **Controlled cycle reintroduction:** compare MST fingerprints against fixed-density alternatives (MST+ m edges, k -NN graphs) to quantify the incremental value of cyclic and mesoscopic structure while preserving comparability; (d) **Physics-guided hybridization:** combine graph fingerprints with contemporaneous heliospheric and geomagnetic covariates (e.g., Dst, solar-wind speed, dynamic pressure, IMF B_z) to evaluate incremental predictive value and improve attribution; and (e) **Rigidity-aware interpretability:** incorporate station metadata (cutoff rigidity, latitude/longitude, altitude) as explicit model inputs or as conditioning variables to clarify how geomagnetic shielding shapes network roles and event fingerprints.

Overall, graph fingerprints provide a compact, interpretable representation of FD morphology that complements standard time-series and index-based analyses. With expanded catalogs, uncertainty quantification, and physics-informed integration, this framework can mature into a practical tool for comparative FD characterization and for probing how heliospheric drivers imprint distinct network signatures on the global neutron-monitor response.

DATA AND CODE AVAILABILITY

NMDB neutron-monitor data are publicly available. The analysis scripts and processed feature tables are available in the repository: <https://github.com/dosquisd/NMDB-FD-PredictorWithGraphs>

ACKNOWLEDGMENTS

We gratefully acknowledge the Dirección de Investigaciones at Universidad Tecnológica de Bolívar for their support and accompaniment throughout this research process. We acknowledge the NMDB database (www.nmdb.eu), founded under the European Union's FP7 programme (contract no. 213007), for providing data.

REFERENCES

- A. Chilingarian, G. Hovsepyan, H. Martoyan, T. Karapetyan, B. Sargsyan, N. Nokolova, H. Angelov, D. Haas, J. Knapp, M. Walter, O. Ploc, J. Shlegl, M. Kakona, and I. Ambrosova, [arXiv e-prints](https://arxiv.org/abs/2212.13514) , [arXiv:2212.13514](https://arxiv.org/abs/2212.13514) (2022), [arXiv:2212.13514](https://arxiv.org/abs/2212.13514) [physics.space-ph].
- K. Ghosh and P. Raychaudhuri, [arXiv e-prints](https://arxiv.org/abs/0701860) , [astro-ph/0701860](https://arxiv.org/abs/0701860) (2007), [arXiv:astro-ph/0701860](https://arxiv.org/abs/0701860) [astro-ph].
- H. V. Cane, *Space Sci. Rev.* **93**, 55 (2000).
- J. J. Blanco, E. Catalán, M. A. Hidalgo, J. Medina, O. García, and J. Rodríguez-Pacheco, *Sol. Phys.* **284**, 167 (2013), [arXiv:1302.2597](https://arxiv.org/abs/1302.2597) [astro-ph.SR].

D.-H. Huang, H.-Q. Hu, J.-L. Zhang, H. Lu, D.-L. Zhang, B.-S. Xue, and J.-T. Lu, [arXiv e-prints](https://arxiv.org/abs/1710.00945), [arXiv:1710.00945](https://arxiv.org/abs/1710.00945) (2017), [arXiv:1710.00945](https://arxiv.org/abs/1710.00945) [astro-ph.HE].

A. Chilingarian, T. Karapetyan, and B. Sargsyan, [arXiv e-prints](https://arxiv.org/abs/2506.17917), [arXiv:2506.17917](https://arxiv.org/abs/2506.17917) (2025), [arXiv:2506.17917](https://arxiv.org/abs/2506.17917) [astro-ph.SR].

A. Bahena Bias and L. Villaseñor, in *Journal of Physics Conference Series*, Journal of Physics Conference Series, Vol. 287 (IOP, 2011) p. 012034.

A. Papaioannou, A. Belov, H. Mavromichalaki, E. Eroshenko, V. Yanke, E. Asvestari, A. Abunin, and M. Abunina, in *Journal of Physics Conference Series*, Journal of Physics Conference Series, Vol. 409 (IOP, 2013) p. 012202.

B. Y. Yushkov, *Advances in Space Research* **77**, 3549 (2026).

T. Laitinen and S. Dalla, *ApJ* **906**, 9 (2021).

G. Ihongo, D. Ruffolo, A. Saiz, U. Tortermpun, and A. C. L. Chian, in *36th International Cosmic Ray Conference (ICRC2019)*, International Cosmic Ray Conference, Vol. 36 (2019) p. 1084.

C. Okany, in *General Assembly and 5th Annual Conference of the African Astronomical Society* (2025) p. 27.

D. Sierra-Porta and A.-R. Domínguez-Monterroza, *Physica A Statistical Mechanics and its Applications* **607**, 128159 (2022).

D. Sierra-Porta, *Chaos* **34**, 023114 (2024).

V. Freitas Silva, M. Eduarda Silva, P. Ribeiro, and F. Silva, *Data Mining and Knowledge Discovery* **39**, [arXiv:2301.02333](https://arxiv.org/abs/2301.02333) (2025), [arXiv:2301.02333](https://arxiv.org/abs/2301.02333) [cs.SI].

V. Freitas Silva, M. Eduarda Silva, P. Ribeiro, and F. Silva, *Wiley Interdisciplinary Reviews: Data Mining and Knowledge Discovery* **11**, [arXiv:2110.09887](https://arxiv.org/abs/2110.09887) (2021), [arXiv:2110.09887](https://arxiv.org/abs/2110.09887) [cs.SI].

J. D. Perez-Navarro and D. Sierra-Porta, *Open Journal of Astrophysics* **9** (2026), [10.33232/001c.157585](https://doi.org/10.33232/001c.157585).

L. Gutierrez Gomez, B. Chiem, and J.-C. Delvenne, [arXiv e-prints](https://arxiv.org/abs/1705.10817), [arXiv:1705.10817](https://arxiv.org/abs/1705.10817) (2017), [arXiv:1705.10817](https://arxiv.org/abs/1705.10817) [stat.ML].

C. Stam, P. Tewarie, E. Van Dellen, E. Van Straaten, A. Hillebrand, and P. Van Mieghem, *International Journal of Psychophysiology* **92**, 129 (2014).

C. T. Steigies, in *Data, Analysis and Software in Heliophysics (DASH) 2023* (2023) p. 19.

C. T. Steigies, in *AGU Fall Meeting Abstracts*, AGU Fall Meeting Abstracts, Vol. 2016 (2016) pp. 1N44A–05.

H. Mavromichalaki, A. Papaioannou, C. Plainaki, C. Sarlanis, G. Souvatzoglou, M. Gerontidou, M. Papailiou, E. Eroshenko, A. Belov, V. Yanke, E. O. Flückiger, R. Bütkofer, M. Parisi, M. Storini, K.-L. Klein, N. Fuller, C. T. Steigies, O. M. Rother, B. Heber, R. F. Wimmer-Schweingruber, K. Kudela, I. Strharsky, R. Langer, I. Usoskin, A. Ibragimov, A. Chilingaryan, G. Hovsepyan, A. Reymers, A. Yeghikyan, O. Kryakunova, E. Dryn, N. Nikolayevskiy, L. Dorman, and L. Pustil'Nik, *Advances in Space Research* **47**, 2210 (2011).

A. S. Shirkhorshidi, S. Aghabozorgi, and T. Y. Wah, *PLoS ONE* **10**, [e0144059](https://doi.org/10.1371/journal.pone.0144059) (2015).

S. Wang, J. G. Yabes, and C.-C. H. Chang, *Journal of Data Science* **19**, 15 (2021).

A. Shifaz, C. Pelletier, F. Petitjean, and G. I. Webb, *Knowledge and Information Systems* **65**, 2665 (2023).

F. R. Chung and L. Lu, *Complex graphs and networks*, 107 (American Mathematical Soc., 2006).

J. Kim and T. Wilhelm, *Physica A: Statistical Mechanics and its Applications* **387**, 2637 (2008).

Y. M. Omar and P. Plapper, *Entropy* **22**, 1417 (2020).

NOAA Space Weather Prediction Center, “Noaa space weather scales (geomagnetic storms g1–g5),” (2024), accessed 2026-02-12.

I. Richardson and H. Cane, *Solar Physics* **270**, 609 (2011).

D. Smart and M. Shea, *Advances in Space Research* **36**, 2012 (2005).

A. Mishev, N. Larsen, E. Asvestari, A. Sáiz, M. A. Shea, D. T. Strauss, D. Ruffolo, C. Banglieng, S. Seunarine, M. L. Duldig, *et al.*, *Advances in Space Research* **74**, 4160 (2024).

G. E. Box and D. R. Cox, *Journal of the Royal Statistical Society Series B: Statistical Methodology* **26**, 211 (1964).

M. Tumminello, C. Corronello, F. Lillo, S. Micciche, and R. N. Mantegna, *International Journal of Bifurcation and Chaos* **17**, 2319 (2007)

provides fast and easy peer review for new papers in the **astro-ph** section of the arXiv, making the reviewing process simpler for authors and referees alike. Learn more at <http://astro.theoj.org>.

This paper was built using the Open Journal of Astrophysics L^AT_EX template. The OJA is a journal which